

promoting access to White Rose research papers



Universities of Leeds, Sheffield and York
<http://eprints.whiterose.ac.uk/>

This is the published version of an article in **Monthly Weather Review, 140 (8)**

White Rose Research Online URL for this paper:

<http://eprints.whiterose.ac.uk/id/eprint/76591>

Published article:

Glaeser, G, Knippertz, P and Heinold, B (2012) *Orographic Effects and Evaporative Cooling along a Subtropical Cold Front: The Case of the Spectacular Saharan Dust Outbreak of March 2004*. Monthly Weather Review, 140 (8). 2520 - 2533. ISSN 0027-0644

<http://dx.doi.org/10.1175/MWR-D-11-00315.1>

Orographic Effects and Evaporative Cooling along a Subtropical Cold Front: The Case of the Spectacular Saharan Dust Outbreak of March 2004

GREGOR GLÄSER

Institute for Atmospheric Physics, Johannes Gutenberg University Mainz, Mainz, Germany

PETER KNIPPERTZ AND BERND HEINOLD

School of Earth and Environment, University of Leeds, Leeds, United Kingdom

(Manuscript received 3 November 2011, in final form 7 February 2012)

ABSTRACT

On 2 March 2004 a marked upper-level trough and an associated surface cold front penetrated into the Sahara. High winds along and behind this frontal system led to an extraordinary, large-scale, and long-lived dust outbreak, accompanied by significant precipitation over parts of Algeria, Tunisia, and Libya.

This paper uses sensitivity simulations with the limited-area model developed by the Consortium for Small-Scale Modeling (COSMO) together with analysis data and surface observations to test several hypotheses on the dynamics of this case proposed in previous work. It is demonstrated that air over central Algeria is cooled by evaporation of frontal precipitation, substantially enhancing winds at the leading edge of the cold front. This process is supported by very dry low-level air in the lee of the Atlas Mountains associated with a foehn situation. Flattening the mountain chain in a sensitivity experiment, however, has complex effects on the wind. While reduced evaporative cooling weakens the front, the elimination of the orographic blocking accelerates its penetration into the Sahara. The simulations also indicate high winds associated with a hydraulic jump at the southern slopes of the Tell Atlas.

Feeding the simulated winds into a dust emission parameterization reveals reduced emissions on the order of 20%–30% for suppressed latent heating and even more when effects of the increased precipitation on soil moisture are considered. In the experiment with the Atlas removed, effects of the overall increase in high winds are compensated by an increase in precipitation. The results suggest that a realistic representation of frontal precipitation is an important requisite to accurately model dust emission in such situations.

1. Introduction

In March 2004 extraordinarily widespread and long-lasting dust emission over large parts of the Sahara, paired with rapid transport to the south and west, led to the creation of an enormous dust plume, which during its final stages covered the subtropical and tropical Atlantic Ocean from Morocco to the Gulf of Guinea. Figure 1 shows the extent of the dust front on 1200 UTC 3 and 6 March. This spectacular case instigated a lot of research interest on the dynamical background, the dust emission and transport, and the dust's impacts on precipitation and aerosol optical depth (Knippertz and Fink 2006,

hereafter KF06; Min et al. 2009; Shao et al. 2010; Mangold et al. 2011). According to Shao et al. (2010), the amount of dust emitted from North Africa during this whole major dust outbreak is in the range of the total annual emission from the Sahara Desert. KF06 analyzed the synoptic evolution of this case in detail. Dust emissions were first observed over central Algeria in connection with the crossing of an upper-level trough and associated surface cold front over the Atlas Mountains. The strong increase in pressure in the cool air behind the front then led to sustained strong northerly flow and dust emission across large parts of the Sahara. Between 1500 and 1800 UTC on 2 March 2004 the central Algerian synoptic station Adrar reported a reduction in visibility to 100 m, a wind speed rise from 9 to 18 m s⁻¹, a temperature drop from 25° to 12°C, a dewpoint rise of 12°C, and a pressure rise of 5.3 hPa. The further development of this dust outbreak was associated with a Harmattan surge

Corresponding author address: Gregor Gläser, Institute for Atmospheric Physics, Johannes Gutenberg University Mainz, Becherweg 21, 55128 Mainz, Germany.
E-mail: glaese@uni-mainz.de

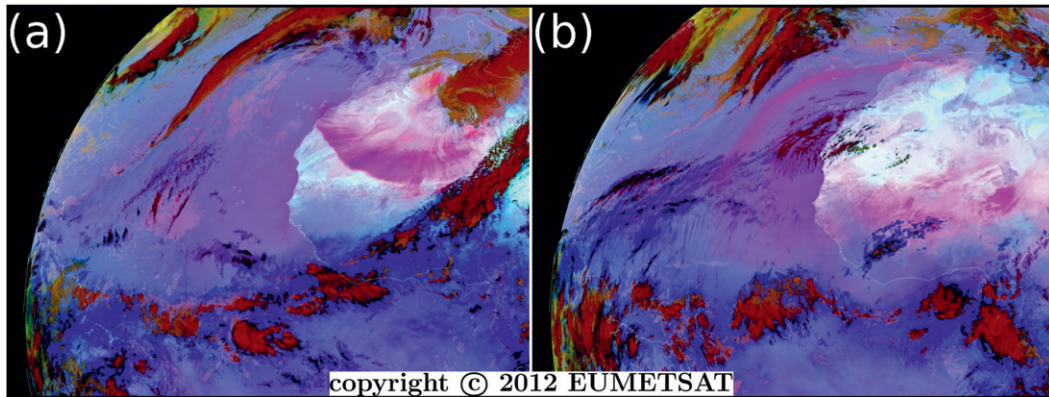


FIG. 1. European Organisation for the Exploitation of Meteorological Satellites (EUMETSAT) Meteosat Second Generation (MSG) dust red–green–blue (RGB) composite for (a) 1200 UTC 3 and (b) 1200 UTC 6 Mar 2004. Airborne dust is indicated by pinkish colors. The RGB composite is produced using the following MSG infrared channels: 12.0–10.8 μm (red), 10.8–8.7 μm (green), and 10.8 μm (blue).

reaching the Guinea Coast, where it caused a breakdown of the land–sea breeze and produced maximum temperature records (KF06).

KF06 hypothesized that the evaporation of cold frontal precipitation south of the Atlas Mountains and the associated increase in density accelerated the low-level winds at the leading edge of the cold front to cause the initial dust mobilization. Such a dualism of cold fronts and density currents is extensively discussed in Smith and Reeder (1988). KF06 further speculated that foehn effects might have enhanced dryness on the lee side, which supported the evaporation.

Studies of idealized cold fronts have shown that diabatic effects can have a considerable impact on the dynamical structure of the front (e.g., Thorpe and Nash 1984; Barth and Parsons 1996). Diabatic effects have been found to modify frontal systems in different ways, causing a more rapid propagation of the front, prefrontal pressure troughs and wind shifts, or prefrontal stable layers that can slow frontal movement (Schultz 2005). Case studies of cold fronts in subtropical or arid regions show that subcloud evaporational cooling can be either frontogenic or frontolytic (Ryan et al. 1989; Katzfey and Ryan 1997; Schultz and Trapp 2003; Chen et al. 2007).

The large interest in cases like the March 2004 event is intimately related to the important role of Saharan dust in the climate system. Mineral dust accounts for about 60% of the global aerosol mass burden (Textor et al. 2006)—about half of which is emitted from the Sahara (Ginoux et al. 2004; Tanaka and Chiba 2006). Once airborne, dust affects radiation (Haywood et al. 2001) and cloud microphysics (Richardson et al. 2007). According to Yin and Chen (2007), the absorption-induced heating in lower-tropospheric dust layers can lead to less cloud cover and less precipitation, while dust particles in altitudes

above the -5°C level may promote the development of clouds and precipitation. Dust provides the strongest signature in the aerosol optical depth and perturbation to the clear sky radiation budget over the ocean and thus poses a challenge to satellite retrieval algorithms (Haywood et al. 1999, 2001). Furthermore, mineral dust particles are known to be efficient ice nuclei (Klein et al. 2010). As such, they can have impacts on the upper parts of cold clouds (Richardson et al. 2007) and on tropical deep convection (Gong et al. 2010). For example, the dust outbreak discussed here influenced the microphysical processes of a deep convective cloud system over the Gulf of Guinea, shifting the size distribution of hydrometeors to smaller particles (Min et al. 2009). Refined treatment of dust in numerical models tends to improve model climatologies and forecast skills. Studies with an advanced aerosol climatology within the European Centre for Medium-Range Weather Forecasts (ECMWF) model show positive effects on the forecasts of the African easterly jet (Tompkins et al. 2005) as well as on the West African monsoon, tropicwide precipitation, and the mean extratropical circulation errors (Rodwell and Jung 2008). Using the National Centers for Environmental Prediction (NCEP) limited-area Eta Model, Pérez et al. (2006) demonstrate significant improvements of the atmospheric temperature and the mean sea level pressure (MSLP) forecasts if the radiative effects of mineral dust are incorporated in the model.

The mobilization of desert dust occurs in sparsely or nonvegetated areas depending on surface properties and is highly dependent on the near-surface wind speed. A certain local threshold value has to be exceeded that depends on the soil particle size (Cornelis et al. 2004). The emission of mineral dust is initiated by the process of saltation, which produces the fine dust particles that can be transported over large distances (Iversen and White

TABLE 1. Setup of COSMO7 and COSMO2.8.

	COSMO7	COSMO2.8
Model version	4.3	4.3
Initial and boundary data	ECMWF analyses	COSMO7 hindcasts
Simulation time span	0000 UTC 1 Mar to 0000 UTC 7 Mar 2004	0600 UTC 2 Mar to 0000 UTC 3 Mar 2004
Horizontal grid spacing	0.0625° \approx 7.0 km	0.025° \approx 2.8 km
No. of grid points	780 \times 632 = 492 960	441 \times 341 = 150 381
Vertical layers	40	40
Time integration scheme	Two-time-level Runge–Kutta	Two-time-level Runge–Kutta
Time step	30 s	30 s
Parameterization of convection	Tiedtke mass flux scheme	Only shallow convection
Ice scheme	Two-category	Three-category

1982). Saltation is approximately proportional to the horizontal friction velocity to the power of 3 (White 1979; Alfaro and Gomes 2001). For the investigation of the miscellaneous consequences of airborne dust and the modeling of the entire dust cycle within numerical models a good handling of the dust emission is essential (Tegen and Fung 1995; Heinold et al. 2008). Improvements in the numerical modeling of the dust cycle therefore require a better understanding of the processes that produce strong surface winds over dust source regions.

The objectives of this paper are therefore to test the hypothesis of KF06 on front intensification through evaporation in the lee of the Atlas and to assess the impacts of this mechanism on dust emission. Since such hypotheses are difficult to test with observational data alone, carefully designed sensitivity experiments with a limited-area numerical model will be carried out to investigate the fully nonlinear effect of subcloud diabatic cooling and the flow across the Atlas Mountains. Moreover, we will look more generally into the effects of the Atlas Mountains for this case, including an investigation of downslope windstorms associated with hydraulic jumps (e.g., Lin 2007) in the lee of the Atlas chain. The remainder of this paper is structured as follows. The numerical model setup, the dust emission model, and the observational data used in this study are described in section 2, followed by an evaluation of the control simulation in section 3. Section 4 contains a detailed analysis of the impact of the evaporative cooling on low-level wind speed distribution and dust emissions, while the influence of the Atlas Mountains is discussed in section 5. A summary and conclusions are provided in section 6.

2. Data and model

a. The COSMO model

In this study we analyze output from the regional, nonhydrostatic model developed by the Consortium for Small-Scale Modeling (COSMO), which is currently

used for operational numerical weather prediction at the German and several other European weather services (Schättler et al. 2008). Details about the setup used in this work are summarized in Table 1. The model was run with horizontal grid spacings of 7 km (COSMO7) and 2.8 km (COSMO2.8) on two different model domains (Fig. 2). COSMO2.8 is nested into COSMO7, which in turn receives initial and boundary data from ECMWF operational analyses (see section 2b). Simulation periods cover 0000 UTC 1 March to 0000 UTC 7 March 2004 for COSMO7 and 0600 UTC 2 March to 0000 UTC 3 March for COSMO2.8. In COSMO7 deep moist convection is parameterized using the Tiedtke mass flux scheme (Tiedtke 1989), while only nonprecipitating shallow convection is parameterized in COSMO2.8. The microphysics packages differ in the number of

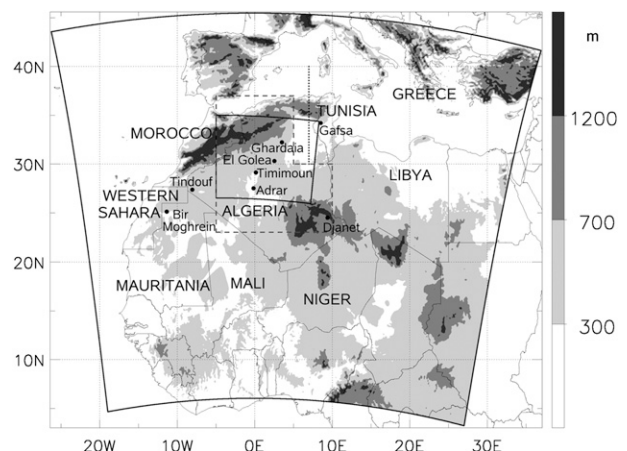


FIG. 2. Model domains of COSMO7 (exterior bold black line) and COSMO2.8 (interior bold black line). The shading shows the topography in meters above mean sea level of COSMO7. Black dots indicate synoptic stations used in this study. The region, where the model is modified in the first sensitivity experiment (NOLATC; see section 4b), is surrounded by a dashed gray line. Thin black lines mark political borders. The bold dotted line indicates the location of the cross section shown in Fig. 8.

TABLE 2. Synoptic stations in North Africa that are used for the evaluation of the CTR (see Fig. 1 for location).

Station name	Country	World Meteorological Organization (WMO) No.	Lat, °N	Lon, °E	Elev, m
Adrar	Algeria	60620	27.53	-0.17	263
Bir Moghrein	Mauritania	61401	25.14	-11.37	360
Djanet	Algeria	60670	24.33	9.28	1054
El Golea	Algeria	60590	30.34	2.52	397
Gafsa	Tunisia	60745	34.25	8.49	314
Ghardaia	Algeria	60566	32.23	3.49	450
Timimoun	Algeria	60607	29.15	0.17	312
Tindouf	Algeria	60656	27.40	-8.08	431

hydrometeor categories. COSMO7 simulates snow and ice, while COSMO2.8 also includes graupel. The simulations with these standard setups are termed control simulations (CTRs). To quantify the impact of orography and evaporation, sensitivity experiments are carried out, which are described in detail in sections 4b and 5a, respectively.

b. Observational and analysis data

ECMWF operational analyses with $1^\circ \times 1^\circ$ grid spacing are used as initial and boundary data of the COSMO model simulations and for the evaluation of the control runs. This dataset is considered to provide a reliable description of the dynamics and thermodynamics of the event (KF06). The model output will also be compared to synoptic surface observations (SYNOPs) of temperature and wind from various stations in North Africa distributed by the World Meteorological Organization (Table 2 and Fig. 2).

c. Dust emission model

For a quantitative estimate of the impact of single meteorological processes on dust emission, a separate model driven by hourly (COSMO2.8) and 6-hourly (COSMO7) model output is used. Time and size resolved dust emission fluxes are computed for the individual COSMO simulations applying the emission parameterization by Tegen et al. (2002) in postprocessing mode, which has been used for mineral dust simulations at the global (Tegen et al. 2004; Stier et al. 2005) and regional scales (Tegen et al. 2006; Heinold et al. 2011). For the dust emission computation, surface friction velocities are calculated from the 10-m model winds, and threshold friction velocities of initial dust mobilization are determined for each soil size fraction. To compensate for the lower surface winds in simulations with COSMO7 and to ensure similar dust emission fluxes for 2.8- and 7-km grid spacing, the emission threshold velocity is reduced by 10% (as also described by Heinold et al. 2007). Potential dust sources are prescribed on the basis of Meteosat Second Generation (MSG) satellite observations of

dust source activations (Schepanski et al. 2007, including updates). Over active sources, the surface roughness is set to a constant value of 0.001 cm.

Soil moisture largely impedes dust emission because of interparticulate capillary forces that adhere single particles to the ground (Fécan et al. 1999). The impact of soil moisture on dust emission is tested here in a very simplistic way. Dust emission is computed in three different ways: (i) assuming no influence of soil moisture, (ii) suppressing dust emission over regions with 1 mm of rain over the previous 24 h, and (iii) same as (ii) but for 5 mm.

3. Evaluation of the control simulation

The first step of the analysis is to evaluate the CTR from COSMO7 with observational data. The model output is interpolated to a regular $1^\circ \times 1^\circ$ grid in order to make it comparable to ECMWF analyses. Figure 3a shows the 500-hPa geopotential height (Z500) as analyzed by ECMWF for 0000 UTC 5 March 2004—that is, during the mature stages of the event, when the upper-level trough extended from southeastern Europe to Niger. Differences between the CTR and the ECMWF analysis for this time, which corresponds to 4 days into the simulation, are very small throughout most of the domain with two notable exceptions. One is a dipole at the southwestern end of the trough over Libya (25°N , 10°E), and the other is an area of slightly lower Z500 in the CTR over the eastern Mediterranean Sea. The root-mean-square error (RMSE) calculated for the area 10° – 40°N , 15°W – 25°E (i.e., 1271 grid points; see box in Fig. 3a) for this time is 8.3 gpm. This area excludes the outer parts of the model domain, where the simulations are nudged to ECMWF data. During the simulation period from 1 to 7 March 2004 the RMSE varies between 3.7 gpm and a maximum of 11.3 gpm at 1200 UTC 4 March 2004. In operational forecasts, RMSEs typically reach about 20 gpm after 2 days (J.-P. Schultz, German Weather Service, 2008, personal communication). This and the lack of a RMSE trend in the COSMO7 simulation indicate that

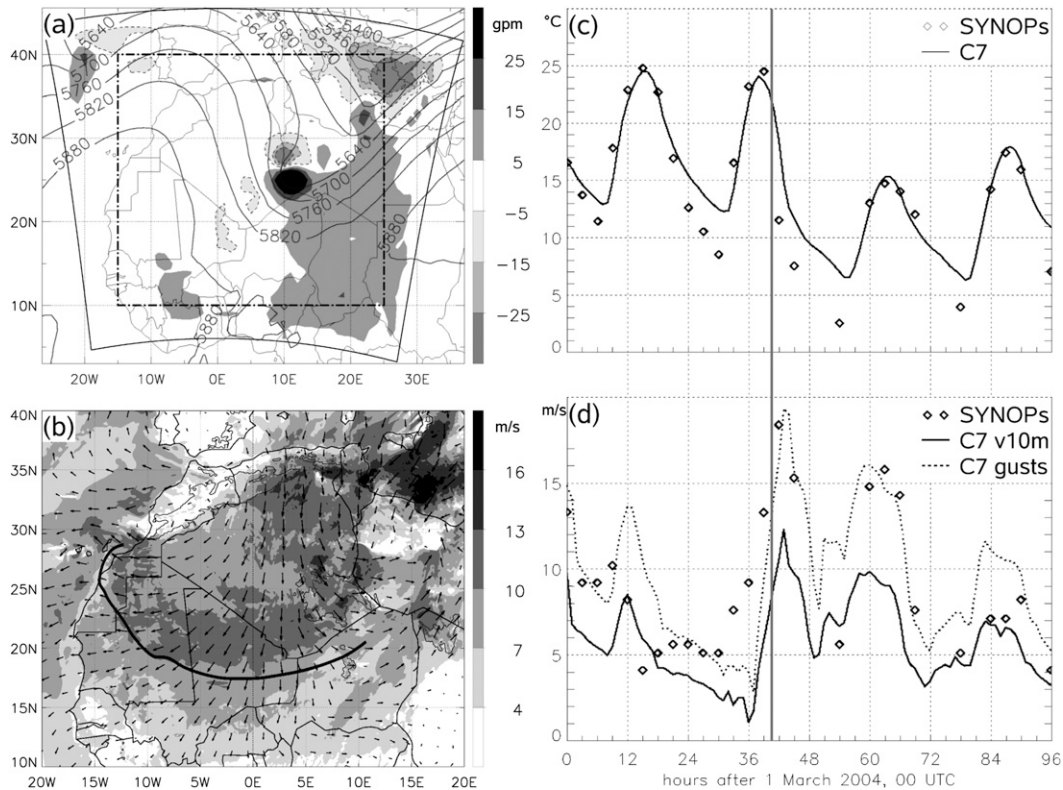


FIG. 3. Evaluation of the CTR (COSMO7). (a) Geopotential height at 500 hPa as analyzed by the ECMWF (contoured every 60 gpm) at 0000 UTC 5 Mar 2004. Shadings (negative values are bordered with dashed lines) show the CTR (interpolated to a $1^\circ \times 1^\circ$ grid) minus ECMWF analysis for the same time, which corresponds to 96 h after initialization. The black dashed-dotted line borders the region of the RMSE calculation. (b) 10-m wind vectors and speed from the CTR at 1200 UTC 3 Mar 2004 (60 h after initialization). The bold black line marks the dust front as subjectively analyzed by KF06 from satellite imagery. (c),(d) Time series of (c) 2-m temperature and (d) 10-m wind speed for 0000 UTC 1 Mar to 0000 UTC 5 Mar. Solid lines show the results of the CTR; diamonds are observations from Adrar. The dotted line in (d) shows the maximum 10-m wind gusts in the model during the past hour. The vertical gray line marks the observed frontal passage in Adrar between 1500 and 1800 UTC on 2 Mar.

the boundary conditions keep the CTR fairly close to the ECMWF analyses throughout the entire period.

Figure 3b shows the horizontal distribution of 10-m wind speed from COSMO7 at 1200 UTC 3 March 2004. There is an extensive, convex-shaped area with winds well above 10 m s^{-1} stretching from the Moroccan coast to the Algerian–Libyan border. The southern and western fringes of this region correspond very well with the leading edge of the dust front as identified and tracked by KF06 from Meteosat satellite imagery (marked with a bold black line in Fig. 3b; see also Fig. 1a). This suggests that the propagation of the cold front and the associated strong winds are well captured by COSMO7. This holds in a similar way for prior and later times (not shown). The second region of high winds in north-central Algeria in Fig. 3b is also an area of dust mobilization according to satellite imagery (see Fig. 1a).

Figures 3c and d show comparisons between observations of 2-m temperature and wind speed at the central

Algerian station Adrar (see Table 1 and Fig. 2) with the corresponding values interpolated from the COSMO7 output grid to the station location. The comparison covers the first 4 days of the simulation from 0000 UTC 1 March to 0000 UTC 5 March 2004. Adrar has a large diurnal cycle of near-surface temperature with an amplitude on the order of 15 K (Fig. 3c). The COSMO model shows close agreement during the day ($<1\text{-K}$ deviation) and too-warm temperatures by up to 4 K during the night. The mean error for the 4 days indicates a warm bias of more than 1 K. A possible reason for this behavior is an insufficient nocturnal radiation inversion caused by too much diffusion in the model (Todd et al. 2008), but a detailed discussion of this problem is beyond the scope of this paper. The dusty cold front reached Adrar at about 1500 UTC 2 March 2004 associated with a temperature drop of 13 K in 3 hours (see KF06 for more details). The frontal passage is slightly delayed in COSMO7 with temperature decreases of 5.3 K between 1500 and 1800 UTC,

of 8.2 K between 1600 and 1900 UTC, and 10.4 K from 1600 to 2000 UTC. On the previous day the decrease between 1600 and 2000 UTC is only 5.2 K, clearly indicating the additional effect of the cold front.

Figure 3d shows the observed 10-min mean 10-m wind speed at Adrar together with the mean and the maximum gust simulated by the model. COSMO generally underestimates the winds with a mean error of -3.18 m s^{-1} , while the gusts agree much better with the observed magnitude (mean error of $+0.67 \text{ m s}^{-1}$). The arrival of the front during the afternoon of 2 March with an observed increase in wind speed from 9 to 18 m s^{-1} between 1200 and 1800 UTC is reasonably captured with model winds at 1900 UTC reaching 12 m s^{-1} (mean) and 19 m s^{-1} (gusts), respectively. In agreement with the temperature data shown in Fig. 3c, the wind time series also suggests a slight delay of the frontal passage in the model. Comparisons with other stations from the region (see Table 2) largely confirm the conclusions drawn from the Adrar data (not shown).

These results indicate that the model delivers a realistic representation of the synoptic-scale evolution of the case, while some more localized and planetary boundary layer effects might not be fully captured. Our successful reproduction of the March 2004 dust outbreak legitimizes further investigations of the event with sensitivity experiments in sections 4 and 5.

4. Impact of latent cooling

In this section the influence of latent cooling on the frontal movement and the low-level wind speed will be investigated with two different approaches: one based on diagnoses of the CTR data (section 4a) and the other based on a sensitivity experiment in which latent cooling is suppressed in the model (section 4b). Section 4c discusses impacts on dust emission.

a. Control simulation

To study the dynamical details of the frontal zone, the high-resolution COSMO2.8 runs are considered. For the diagnostic part, a new model variable dT_{dp} is defined that contains the total temperature tendency due to all phase changes of water accumulated to 1 h. Main contributions to this parameter come from the cloud microphysics scheme and the saturation adjustment. Figure 4a shows dT_{dp} between 1700 and 1800 UTC on 2 March 2004 in a north–south vertical cross section across the cold front from 27° to 33°N along 4°E (see line A–B in Fig. 4b). The black line, which borders the area where the sum of the mixing ratio of all hydrometeor types (rain, snow, and graupel) exceeds 1 g kg^{-1} , is used to delineate thick cloud and precipitation. Three different

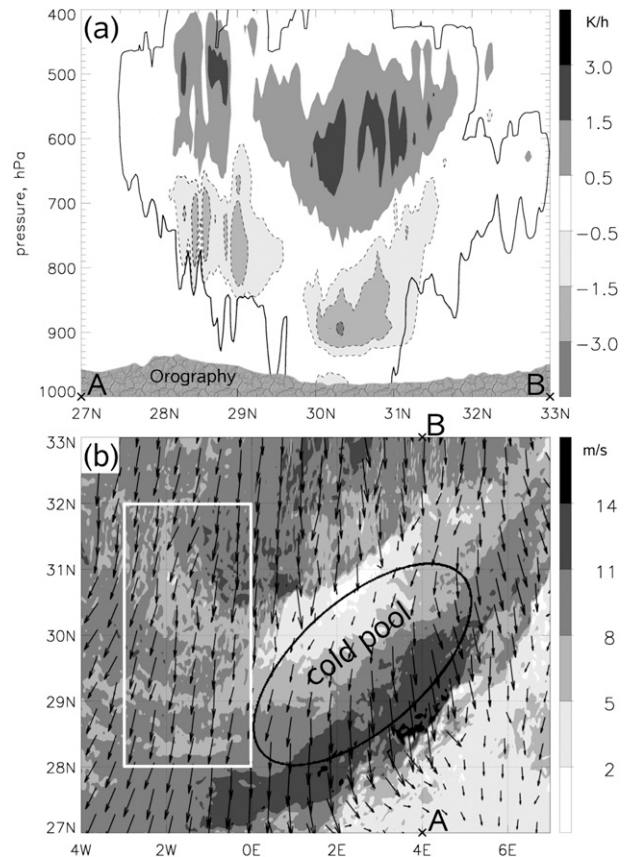


FIG. 4. Cold pool generation in the CTR (COSMO2.8) at 1800 UTC 2 Mar. (a) Diabatic heating rate (shading; negative values are bordered with dashed lines) in a vertical cross section along 4°E from 27° to 33°N . The black line indicates where the sum of specific rain, snow, and graupel content exceeds 1 g kg^{-1} . (b) 10-m wind vectors and speed (shading) for the same time. A black ellipse marks the cold pool, while a white rectangular box borders the region used to characterize "undisturbed flow" (see text for more details).

zones can be distinguished: 1) Between 32° and 33°N clouds are rather shallow (mainly 700–600 hPa) and not associated with large values of dT_{dp} . 2) The main frontal zone, which lies between 32° and 29.5°N , shows a much deeper layer of high hydrometeor concentrations. Between 720 and 470 hPa, dT_{dp} indicates substantial latent heating through condensation, freezing, and resublimation with values of up to 2.5 K h^{-1} . Below the cloud base, which is around 770 hPa in this area, is a region of even larger negative dT_{dp} due to evaporation, melting, and sublimation of hydrometeors in the dry desert air. At about 940 hPa, the subcloud air becomes moist enough so that the remaining precipitation can reach the ground. 3) Between 29.5° and 27.5°N , the area of high hydrometeor concentration and the cloud base rise to about 650 hPa. A smaller, slightly weaker, and more elevated couplet of positive and negative dT_{dp}

is found in the center of this region, indicating that all precipitation evaporates before reaching the ground.

The corresponding 10-m wind field is shown in Fig. 4b. There is a clear frontal structure stretching from circa 27°N, 1°W to 30°N, 5°E with maximum values of more than 14 m s^{-1} near 28.5°N, 4°E. In the central and eastern part of the domain, where the wind change at the front is sharpest, a conspicuous decrease in wind speed occurs behind the front down to values of less than 2 m s^{-1} . To the west of 0° the flow is much more uniform, especially within the white box in Fig. 4b. The mean 10-m wind speed in this region is 8.6 m s^{-1} . If one assumes this to be a representative background flow, the positive and negative signal in the wind field between 2° and 4°E would be on the order of 6 m s^{-1} . Such a pattern is consistent with the horizontal spreading of a pool of evaporatively cooled and therefore denser air (marked in Fig. 4b) superposed on a northerly background flow. The horizontal flow of air out of the cold pool is also reflected in the wind direction. According to the MSLP field (see Fig. 5a), the geostrophic wind direction over the domain is mostly northeasterly. Over the western parts, the flow is deflected by surface friction to become north-northeast (Fig. 4b). In the area of the maximum wind speed, a westerly component away from the assumed cold pool is evident. The wind field is generally less coherent in this region, which is consistent with disturbances generated by evaporatively driven downdrafts. The same mechanism turns the wind vectors into a more northeasterly direction on the northwestern side of the cold pool. Here, however, the wind field is smoother, indicating weaker downdrafts in the moister postfrontal region.

To further discuss the idea of a modification of the frontal flow through evaporatively cooled air, the following thought experiment is conducted. Starting from homogeneous conditions, it is assumed that the cooling diagnosed in Fig. 4a persists for 1 h and that the resulting cold pool subsequently spreads into a resting environment. This estimate will give a rough idea of the accelerations and decelerations associated with the cold pool. The net negative buoyancy of an air parcel below the cloud base in Fig. 4a can be determined by

$$B = g \left(\frac{d\Theta}{\Theta_s} + 0.61 dq_v - q_c - q_r \right), \quad (1)$$

where $d\Theta(dq_v)$ is the difference in potential temperature (water vapor mixing ratio) between the air mass and its surroundings; Θ_s is the ambient potential temperature; q_c and q_r are the mixing ratios of cloud water and rainwater, respectively; and g is the gravitational constant (Weisman and Rotunno 2004). The difference in

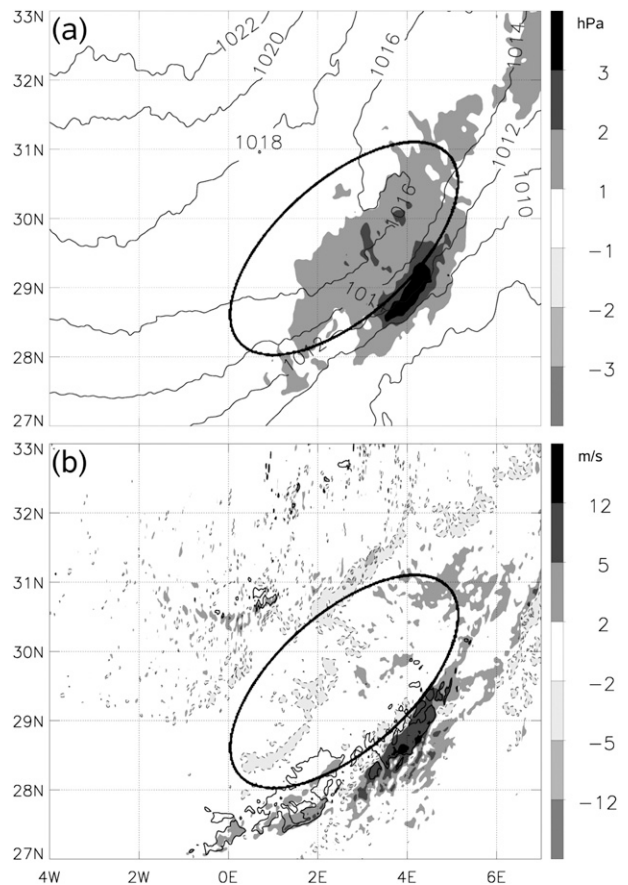


FIG. 5. The role of evaporative cooling. Shown are differences between the CTR minus NOLATC (COSMO2.8) at 1800 UTC 2 Mar 2004 for (a) MSLP and (b) 10-m wind speed (negative values are bordered with dashed lines). Isolines illustrate the absolute values in the CTR [labeled in hPa in (a); 12.5 m s^{-1} contour in (b)]. The cold pool is marked as in Fig. 4b.

temperature due to diabatic processes dT_{dp} is converted to the potential temperature increment $d\Theta$. A constant value of 290 K is assumed for Θ_s . The dominant contribution in this equation comes from the first term with cooling rates of more than 3 K h^{-1} (see Fig. 4a). The concomitant uptake of humidity compensates part of the cooling effect, but is about one order of magnitude smaller. Effects of q_c and q_r are another order of magnitude smaller. Assuming symmetry along the front, the net buoyancy B can be related to the speed of propagation c of a two-dimensional gravity current through

$$c^2 = 2 \int_0^H -B dz, \quad (2)$$

where H represents the depth of the cold pool (Weisman and Rotunno 2004) or, in other words, the vertical level where dT_{dp} goes to zero for a given grid point in Fig. 4a.

If we calculate c in this way for every grid point and average over the ellipsoidal cold pool sketched in Fig. 4b, which features the grid points with the maximum c values in its center, a value of 6 m s^{-1} is obtained. Considering the horizontal scale of about $75\,000 \text{ km}^2$, this is an impressively high value for a cooling period of only 1 h and therefore in good qualitative agreement with the wind modifications discussed above. Note that maximum winds behind the leading edge of a density current are even stronger than the mean propagation speed of the system (Smith and Reeder 1988). This analysis strongly suggests that the large evaporational cooling associated with the penetration of a precipitating cold front into the dry Sahara Desert can substantially modify the wind structure at the front.

b. Sensitivity experiment NOLATC

To test the hypothesis discussed in the previous subsection in a fully nonlinear modeling framework, a sensitivity experiment is carried out where evaporation, melting, and sublimation are suppressed below the cloud base throughout the entire simulation period. For COSMO7 this modification is only applied in the horizontal domain marked with a dashed gray line in Fig. 2 to minimize effects from outside the main cold front/cold pool region. The results of this simulation are then used as initial and boundary data for the COSMO2.8 simulation where the modifications are applied in the entire model domain. This simulation will be referred to as sensitivity experiment *no latent cooling* (NOLATC) in the following.

Figure 5a shows the difference in MSLP between the CTR and NOLATC together with the absolute values from the CTR for 1800 UTC 2 March 2004, which is the same time as in Fig. 4. There is a strong southeast–northwest-oriented MSLP gradient across the domain. The gradient is clearly sharpened in the region of the cold pool (indicated with the same ellipse as in Fig. 4b) with the 1016-hPa contour bulging much farther southeastward than in the surroundings. The differences between the two runs show a broad region with values of just above 1 hPa in the area of the cold pool. Differences abruptly increase to over 3 hPa at the southeastern fringe of this region over a stretch of about 100 km. This suggests that the cold pool in the CTR substantially sharpens and accelerates the front in this area. The cross section shown in Fig. 4a cuts right through this part of the front. The impact of these MSLP differences on the 10-m wind field is shown in Fig. 5b. The 12.5 m s^{-1} isotach from the CTR (black line) largely follows the main frontal zone as seen in Fig. 4b. The suppression of the cold pool in the model in NOLATC reduces wind speeds along the entire front by more than 10 m s^{-1} in

TABLE 3. Total dust emission in Mt in the region 27° – 33° N, 4° W– 7° E (domain of Fig. 4) between 1200 UTC 2 Mar and 0000 UTC 3 Mar 2004. Values are given for the CTR and the two sensitivity experiments for different model grid spacings and 24-h precipitation thresholds for dust suppression. In parentheses the relative difference to the CTR is given.

Δx	RR _{thr}	CTR	NOLATC	NOATL	
2.8 km	—	1.14	0.92	(−19%)	
7.0 km	—	1.15	0.76	(−34%)	1.43 (+24%)
7.0 km	5 mm	1.15	0.74	(−36%)	1.10 (−4%)
7.0 km	1 mm	0.92	0.32	(−65%)	0.56 (−39%)

places. Not surprisingly, the largest values in Fig. 5b are located in close proximity to the strongest signal in the difference of the MSLP around 29° N, 4° E (Fig. 5a). Within and to the north of the cold pool, the outflow of cold air decelerates the northerly background flow in the CTR, but this effect is much smaller in magnitude than the acceleration farther to the southeast. Overall the signals are on the same order of magnitude as discussed in the previous subsection, but the asymmetry in the signal suggests that the fully nonlinear response is more complicated than a simple superposition of homogeneous background flow with a symmetric cold pool circulation.

c. Impacts on dust emission

Feeding the 10-m winds from the CTR and NOLATC into the offline dust emission parameterization described in section 2c allows for a quantitative statement about the influence of the evaporational cooling and precipitation on dust production along the front. Table 3 gives total dust emissions over the area 27° – 33° N, 4° W– 7° E between 1200 and 2400 UTC on 2 March 2004. Before this time very little dust is lofted in this region. For COSMO2.8 the CTR winds lead to an emission of 1.14 megatons (Mt) over this 12-h period. Suppression of latent cooling leads to a reduction of 19%. This result is sensitive to the grid spacing. For COSMO7, the CTR gives emissions of 1.15 Mt (recall that some tuning was applied to match emission from the two different grid spacings; see section 2c). The reduction in NOLATC is now even more substantial with a value of 0.76 Mt (−34%).

Precipitation is very scarce in the Sahara Desert and the soil moisture is usually very low. In this case, however, rainfall was observed and simulated. Including the impact of soil moisture, the differences between the CTR and NOLATC further increase because of the fact that more precipitation reaches the ground in NOLATC. If dust emission is suppressed at grid points where the precipitation in the last 24 h was $\geq 5 \text{ mm}$ (1 mm), the difference between the two experiments increases to 36% (65%). This way, evaporational cooling supports

dust emission by both accelerating winds and keeping the soil dryer.

5. Impact of the Atlas Mountains

This section investigates the influence of the Atlas Mountains on the evolution of the dust front on 2 and 3 March 2004 using a combination of diagnostic and sensitivity experiment approaches as in the previous section. In section 5a, aspects such as the influence of the mountains on frontal propagation, the generation of a foehn situation, and lee cyclogenesis will be discussed. Section 5b will then examine the potential of downslope windstorms and hydraulic jumps. Impacts on dust emission will be discussed at the end of each subsection.

First of all, it is notable that only the COSMO7 model domain includes the entire Atlas Mountains. COSMO2.8 better resolves orographic details, but as the windward side of the mountains is outside of the model domain, the foehn is mainly driven by the COSMO7 boundary conditions. On the lee side, the 2-m temperature, dewpoint, and humidity hardly differ between the CTRs of COSMO2.8 and COSMO7, while the maximum wind speeds along the front are 1–2 m s^{-1} higher in COSMO2.8. Also, rain rates are higher in COSMO2.8 on the lee side, which enhances the impact of precipitation on dust emission, as discussed in the end of section 5a. To include the driving factors of the foehn and, as the interest in this case is on synoptic to mesoscale effects, further analyses are restricted to COSMO7.

a. Sensitivity experiment NOATL

To investigate the full nonlinear response of the atmospheric flow to the existence of the Atlas Mountains, a second sensitivity experiment *no Atlas Mountains* is carried out (referred to as NOATL). In NOATL the model orography is flattened in the region of the Atlas by linearly interpolating from a line from 25°N, 12°W to 34°N, 10°E northward to the North African coast line (Fig. 6).

Again for 1800 UTC 2 March 2004, Fig. 7 shows differences of the CTR minus NOATL of 2-m dewpoint temperature (ΔT_d), total precipitation of the past 6 h (ΔRR), MSLP (ΔMSLP), and 10-m wind speed ($\Delta v_{10\text{m}}$) together with selected absolute values from the CTR as in Fig. 5. The first thing to note is a blocking of the northerly cold air advection in the CTR resulting in a positive ΔMSLP signal east of 5°W (Fig. 7c). The forced ascent of nonblocked air is associated with orographic rainfall enhancement in the CTR reaching up to 6 mm close to the northern Algerian Mediterranean coast (Fig. 7b). As a consequence, the air in the lee is much drier with ΔT_d reaching values of less than -15 K around 32°N, 5°E

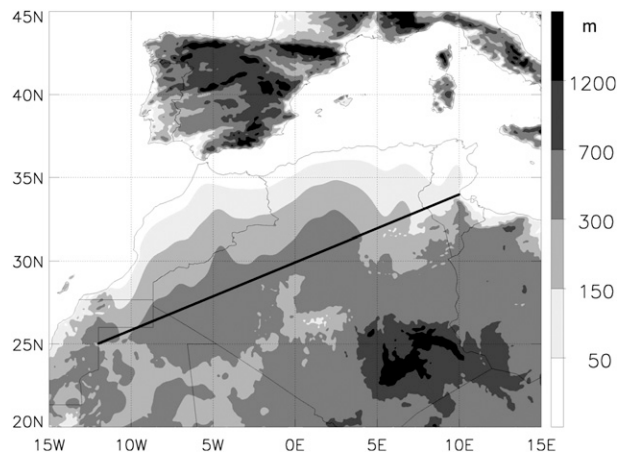


FIG. 6. The model orography for the NOATL sensitivity experiment is flattened in the region of the Atlas by linearly interpolating from the black line (25°N, 12°W to 34°N, 10°E) northward to the North African coast line.

(Fig. 7a), clearly corroborating a foehn situation in the CTR as hypothesized by KF06. The enhanced dryness at low levels increases the potential for evaporation and thereby reduces precipitation by as much as 6 mm in the CTR as compared to NOATL (Fig. 7b). The resulting intensified cold pool in the CTR is clearly reflected in positive ΔMSLP up to 6 hPa (Fig. 7c) accompanied by $\Delta v_{10\text{m}}$ as large as 6 m s^{-1} (Fig. 7d) to the southeast of the signal in ΔRR (i.e., around 29°N, 6°E). There is a clear structural similarity to the results of NOLATC shown in Fig. 5, but the pattern is shifted by 2°–3° to the east and the negative signal in $\Delta v_{10\text{m}}$ to the northwest of the cold pool is larger in this case.

A striking feature in the $\Delta v_{10\text{m}}$ distribution is the contiguous, convex band of negative values reaching from about 28°N, 8°W to 27°N, 5°E (Fig. 7d). This is an indication that the cold front propagates inland faster and is more intense in NOATL than in the CTR. This shift appears to be closely connected to an extended negative signal in ΔMSLP of up to -6 hPa to the south of the High Atlas Mountains (Fig. 7c), which is a clear sign of lee cyclogenesis in the CTR. The circulation associated with this feature opposes the generally northerly flow on its southeastern side over western Algeria, leading to a deceleration of winds in the CTR there. A corresponding acceleration is found on the northwestern side of the lee cyclone, just off the coast of Morocco (Fig. 7d). This circulation is also reflected in ΔT_d (Fig. 7a), indicating that the advection of cold and moist air from the north is inhibited in the CTR in the region southeast of the lee cyclone while it is enhanced to the northwest of it. This way the removal of the orographic barrier in NOATL allows a more unimpeded penetration of the cold front into the continent.

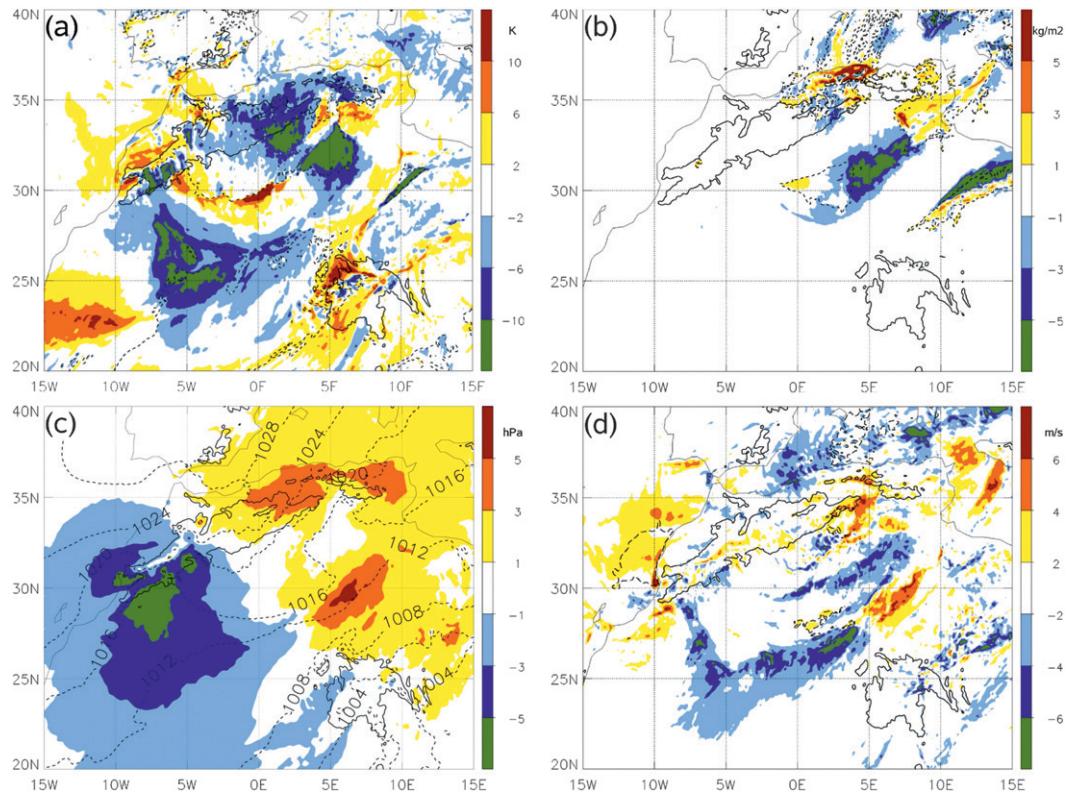


FIG. 7. Role of the Atlas Mountains. Shown are differences between the CTR minus NOATL (COSMO7) at 1800 UTC 2 Mar 2004 (shading). Dashed lines show the absolute values in the CTR in each panel. (a) T_d (-5°C contour), (b) total precipitation of the past 6 h (contour 1 mm), (c) MSLP (contours labeled in hPa), and (d) 10-m wind velocity (contour 12.5 m s^{-1}). Solid lines mark the 1000-m elevation.

NOATL confirms the hypothesis by KF06 that foehn effects support the flow acceleration at the front through enhanced evaporation. However, negative values over large parts of the northern Sahara in Fig. 7d demonstrate higher 10-m wind speeds in NOATL because of the absence of the mountains.

The effect on dust emission is summarized in Table 3. Twenty-four percent more dust is emitted in NOATL than in the CTR if only wind effects are considered. However, when including the effect of the increased precipitation in NOATL on emissions, the signal is reversed. For a threshold of 5 mm in the last 24 h, the CTR and NOATL produce almost the same total emission. Reducing the threshold to 1 mm, NOATL produces substantially less dust emission than the CTR (-39%). This demonstrates that the removal of the Atlas Mountains influences dust emission positively through a more unimpeded penetration of high winds into the continent and negatively through an enhanced moistening of the soil by stronger frontal precipitation. The enhancement in the CTR through drier air and thus more evaporation in the lee, suggested by KF06, is only local and overcompensated by other effects.

b. Formation of a hydraulic jump

The difference in 10-m wind speed between the CTR and NOATL (Fig. 7d) shows a number of areas over and to the south of the Algerian Atlas where the mountains cause higher near-surface wind speeds in the CTR. The large signal to the south of 35°N along 4.5°E is probably related to the channeling of the low-level flow through a gap in the Saharan Atlas in this region (see 1000-m elevation in black in Fig. 7). In the previous subsection we discussed the partial blocking of air in the CTR (see ΔMSLP in Fig. 7c for example), which implies accumulation of potential energy on the windward side of the mountain ridge and, for reasons of continuity, conversion into kinetic energy behind it, leading to high velocities in a shallow layer over the lee slope (Lin 2007). This shallow layer represents an unstable state that re-establishes stable conditions (deeper layer and lower velocity) in a turbulent process: the hydraulic jump. In such a situation, isentropes usually bend downward behind the ridge and rise suddenly at the position of the jump (Miller and Durran 1991; Liu et al. 2000). For 1200 UTC 3 March 2004, when the northerly flow toward

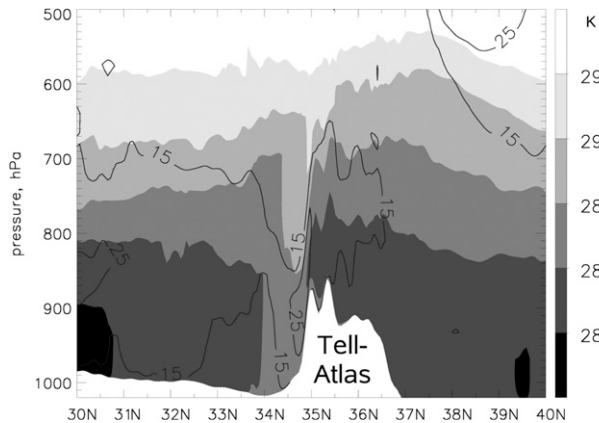


FIG. 8. Hydraulic jump at the Tell Atlas at 1200 UTC 3 Mar 2004. Vertical cross section along 7°E from 30° to 40°N (see Fig. 2 for location) showing potential temperature of the CTR (COSMO7; shading) and 15 m s⁻¹ and 25 m s⁻¹ isotachs (black lines). Topography is shown in white.

the Tell Atlas is strongest, a north–south height cross section along 7°E using COSMO7 data clearly shows such a pattern (Fig. 8). Over the ridge at 35°N, the 288-K isentrope is located at 700 hPa. It then drops to 850 hPa over the lee slope before rising again to 700 hPa. In the region where the 288-K isentrope reaches its lowest level, the wind velocity has a maximum of more than 25 m s⁻¹ directly above the lee slope. Farther south the wind rapidly decreases to values of less than 15 m s⁻¹, which is indicative of a hydraulic jump.

Lin (2007, p. 33) describes five fundamental regimes of flows over mountains based on the Froude number F and the nondimensional mountain height M according to

$$F = \frac{U}{\sqrt{gH}} \quad \text{and} \quad (3)$$

$$M = \frac{h_m}{H}, \quad (4)$$

with U the velocity and H the layer depth of the undisturbed upstream flow, g the gravitational constant, and h_m the mountain height. Figure 8 shows that typical values in the model are on the order of $U = 14 \text{ m s}^{-1}$, $H = 1500 \text{ m}$, and $h_m = 1300 \text{ m}$, resulting in $F = 0.12$ and $M = 0.87$. These values for F and M describe a flow in the regime with a stationary hydraulic jump downstream of the mountain. This result remains valid for U , varying from 10 to 15 m s⁻¹ and H between 1300 and 1700 m. Apart from the region discussed here, little evidence for hydraulic jumps is found in the model, which is most likely related to the less steep southern slopes of the Sahara Atlas (see topography in Fig. 2).

The diagnostic dust model shows very high dust emission fluxes of 15 521 kg s⁻¹ over the lee slope (34°–35°N, 6°–8°E) at 1200 UTC 3 March (not shown). This is 38% of the emission that the CTR simulates in the frontal region at 1800 UTC 2 March. However, emissions decrease to 5000 kg s⁻¹ if suppressed at grid points with more than 1 mm precipitation during the last 24 h. The simulated rainfall is consistent with observations at the nearby meteorological station Gafsa (34.25°N, 8.49°E), where 16-mm precipitation was recorded between 1800 UTC 2 March and 0000 UTC 3 March. Gafsa and other stations in this region did not report dust mobilization on this day. Unfortunately, clouds cover the area to the immediate south of the Tell Atlas on 3 March (Fig. 1a) so that there is no information on dustiness from space. Overall, the analysis suggests that the formation of a hydraulic jump and the accompanying strong low-level winds have the potential to mobilize huge amounts of dust over the lee slope of the Tell Atlas. In this particular case, however, precipitation impedes dust emission to a large extent.

6. Discussion and conclusions

In this paper several dynamical aspects of the spectacular Saharan dust outbreak in March 2004 have been investigated based on numerical simulations with a regional model using 7- and 2.8-km grid spacing. The control simulation compares well with surface data, the ECMWF initial analyses, and satellite images on the meso- to synoptic scale. However, the model struggles to reproduce the very strong nocturnal inversion over the desert observed at synoptic stations, which causes too-high 2-m temperatures during night and in the morning hours. The dynamical analysis is done using a combination of diagnostic investigations and sensitivity experiments with the model. The focus of the study was on understanding the processes that led to the very strong winds on the southern side of the Atlas Mountains during the early stages of the event. KF06 hypothesized that evaporational cooling and a foehn situation were crucial for triggering the initial dust emission.

Some of the main findings are schematically summarized in Fig. 9. Cold frontal precipitation falls into the very dry Saharan air and evaporates, enhancing the temperature contrast across the front and thereby accelerating the near-surface winds at the front, while decelerating the winds to the north of the precipitation zone. This effect enhances dust mobilization along the front in the model. Sensitivity experiments suggest a decrease in dust emission flux by about 20%–30% when subcloud evaporation of precipitation is suppressed. This reduction increases substantially if effects of an additional moistening of the

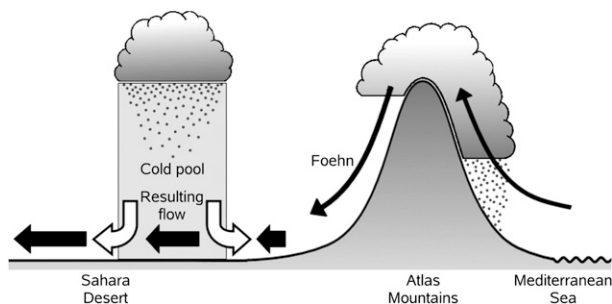


FIG. 9. Schematic diagram showing the formation of the cold pool over the Sahara. The low-level air on the lee side of the Atlas Mountains is additionally dried by foehn effects. Thick black arrows show the superposition of the background wind and the cold pool circulation. Note that nonlinear effects lead to asymmetries resulting in strong winds at the southern side of the cold pool.

soil are taken into account. At least for the very early stages of the event and parts of the cold frontal area, the analysis presented here confirms KF06, who hypothesized that evaporation of cold frontal precipitation accelerated the low-level winds at the leading edge of the front.

The comparison of the CTR with results of another sensitivity study, in which the Atlas Mountains were removed, reveals that cold air is partially blocked by the orographic barrier and partially forced to ascend, leading to enhanced rainfall on the windward side in the CTR. This, in turn, creates a foehn effect in the CTR and thus drier air masses and more evaporation in the lee, resulting in less precipitation, a more distinct cold pool, and stronger frontal winds. However, the mountains also create a lee cyclone farther to the west that slows the winds and the penetration of the cold front over Algeria. These compensating effects hinder a straightforward interpretation of the role of the Atlas Mountains for this dust event. If only wind effects are considered, dust emission is reduced because of the mountains. If effects of the increased inland precipitation in NOATL are taken into account as well, the wind effects can be compensated or even overcompensated depending on the choice of rainfall/soil moisture thresholds. In addition, the model provides evidence for a hydraulic jump at the Tell Atlas with near-ground wind velocities of 25 m s^{-1} . However, it is rather unlikely that these winds mobilized large amounts of dust because the soil in this area was wet from previous rainfall.

In the future it would be interesting to apply the methods developed here to comparable large-scale dust outbreaks such as the ones that occurred in early March 2006 (Slingo et al. 2006; Tulet et al. 2008) and 2007 to see how robust our findings are. In a third sensitivity study, the influence of the Mediterranean Sea could be investigated. Sensible heat fluxes from the relatively warm sea surface to the colder northern airstream potentially

destabilize the lower troposphere, causing a deeper boundary layer. An experiment with reduced sea surface temperatures would help to understand how changes of boundary layer height and stratification affect the flow across the Atlas and the inland penetration of the cold front. Another important extension of this work would be to simulate this case with an online dust model to test effects of radiative feedbacks between dust and dynamics, particularly on the later stages of the event. Stanelle et al. (2010) simulated the dust episode in March 2006 using the online modeling system COSMO-Aerosols and Reactive Trace gases (ART) and showed that the early stages of the event with a strong decrease in 2-m temperature were dominated by the passage of the cold front and not by dust radiative effects. It should also be investigated to what extent coarser-resolution dust models are capable of capturing the processes along the cold front discussed here. Simulations of the March 2004 dust outbreak with the Global and regional Earth-system Monitoring using Satellite and in-situ data (GEMS) aerosol modeling system reveal that the assimilation of Moderate Resolution Imaging Spectroradiometer (MODIS) aerosol optical depth improves the model performance significantly, suggesting that the model underestimates the dust emission in the Sahara (Mangold et al. 2011). This study has shown that an accurate treatment of orographic and diabatic effects in models has the potential to improve simulations of synoptic-scale dust outbreaks.

Acknowledgments. The authors would like to acknowledge funding through the German Science Foundation (DFG) Emmy Noether program (Grant KN 581/2–3) to PK. We thank the anonymous reviewers for their constructive criticism and the DWD for supporting the use of the COSMO model and for providing the necessary external parameters. We are grateful to Klaus Stephan and Florian Meier for help with outputting and modifying diabatic processes.

REFERENCES

- Alfaro, S. C., and L. Gomes, 2001: Modeling mineral aerosol production by wind erosion: Emission intensities and aerosol size distributions in source areas. *J. Geophys. Res.*, **106** (D16), 18 075–18 084.
- Barth, M. C., and D. B. Parsons, 1996: Microphysical processes associated with intense frontal rainbands and the effect of evaporation and melting on frontal dynamics. *J. Atmos. Sci.*, **53**, 1569–1586.
- Chen, G. T. J., C. C. Wang, and A. H. Wang, 2007: A case study of subtropical frontogenesis during a blocking event. *Mon. Wea. Rev.*, **135**, 2588–2609.
- Cornelis, W. M., D. Gabriels, and R. Hartmann, 2004: A parameterisation for the threshold shear velocity to initiate deflation of dry and wet sediment. *Geomorphology*, **59** (1–4), 43–51, doi:10.1016/j.geomorph.2003.09.004.

- Fécan, F., B. Marticorena, and G. Bergametti, 1999: Parametrization of the increase of the aeolian erosion threshold wind friction velocity due to soil moisture for arid and semi-arid areas. *Ann. Geophys.*, **17**, 149–157.
- Ginoux, P., J. M. Prospero, O. Torres, and M. Chin, 2004: Long-term simulation of global dust distribution with the GOCART model: Correlation with North Atlantic Oscillation. *Environ. Modell. Software*, **19**, 113–128, doi:10.1016/S1364-8152(03)00114-2.
- Gong, W., Q. Min, R. Li, A. Teller, E. Joseph, and V. Morris, 2010: Detailed cloud resolving model simulations of the impacts of Saharan air layer dust on tropical deep convection—Part 1: Dust acts as ice nuclei. *Atmos. Chem. Phys. Discuss.*, **10**, 12 907–12 952.
- Haywood, J. M., V. Ramaswamy, and B. J. Soden, 1999: Tropospheric aerosol climate forcing in clear-sky satellite observations over the oceans. *Science*, **283**, 1299–1303, doi:10.1126/science.283.5406.1299.
- , P. N. Francis, M. D. Glew, and J. P. Taylor, 2001: Optical properties and direct radiative effect of Saharan dust: A case study of two Saharan dust outbreaks using aircraft data. *J. Geophys. Res.*, **106** (D16), 18 417–18 430.
- Heinold, B., J. Helmert, O. Hellmuth, R. Wolke, A. Ansmann, B. Marticorena, B. Laurent, and I. Tegen, 2007: Regional modeling of Saharan dust events using LM-MUSCAT: Model description and case studies. *J. Geophys. Res.*, **112**, D11204, doi:10.1029/2006JD007443.
- , I. Tegen, K. Schepanski, and O. Hellmuth, 2008: Dust radiative feedback on Saharan boundary layer dynamics and dust mobilization. *Geophys. Res. Lett.*, **35**, L20817, doi:10.1029/2008GL035319.
- , and Coauthors, 2011: Regional modelling of Saharan dust and biomass-burning smoke Part I: Model description and evaluation. *Tellus*, **63B**, 781–799, doi:10.1111/j.1600-0889.2011.00570.x.
- Iversen, J. D., and B. R. White, 1982: Saltation threshold on Earth, Mars and Venus. *Sedimentology*, **29**, 111–119.
- Katzfey, J. J., and B. F. Ryan, 1997: Modification of the thermodynamic structure of the lower troposphere by the evaporation of precipitation: A GEWEX cloud system study. *Mon. Wea. Rev.*, **125**, 1431–1446.
- Klein, H., and Coauthors, 2010: Saharan dust and ice nuclei over Central Europe. *Atmos. Chem. Phys.*, **10**, 211–221, doi:10.5194/acp-10-2021-2010.
- Knippertz, P., and A. H. Fink, 2006: Synoptic and dynamic aspects of an extreme springtime Saharan dust outbreak. *Quart. J. Roy. Meteor. Soc.*, **132**, 1153–1177, doi:10.1256/qj.05.109.
- Lin, Y., 2007: *Mesoscale Dynamics*. Cambridge University Press, 630 pp.
- Liu, M., D. L. Westphal, T. R. Holt, and Q. Xu, 2000: Numerical simulation of a low-level jet over complex terrain in southern Iran. *Mon. Wea. Rev.*, **128**, 1309–1327.
- Mangold, A., and Coauthors, 2011: Aerosol analysis and forecast in the European Centre for Medium-Range Weather Forecasts Integrated Forecast System: 3. Evaluation by means of case studies. *J. Geophys. Res.*, **116**, D03302, doi:10.1029/2010JD014864.
- Miller, P. P., and D. R. Durran, 1991: On the sensitivity of down-slope windstorms to the asymmetry of the mountain profile. *J. Atmos. Sci.*, **48**, 1457–1473.
- Min, Q. L., R. Li, B. Lin, E. Joseph, S. Wang, Y. Hu, V. Morris, and F. Chang, 2009: Evidence of mineral dust altering cloud microphysics and precipitation. *Atmos. Chem. Phys.*, **9**, 3223–3231.
- Pérez, C., S. Nickovic, G. Pejanovic, J. M. Baldasano, and E. Özsoy, 2006: Interactive dust-radiation modeling: A step to improve weather forecasts. *J. Geophys. Res.*, **111**, D16206, doi:10.1029/2005JD006717.
- Richardson, M. S., and Coauthors, 2007: Measurements of heterogeneous ice nuclei in the western United States in springtime and their relation to aerosol characteristics. *J. Geophys. Res.*, **112**, D02209, doi:10.1029/2006JD007500.
- Rodwell, M. J., and T. Jung, 2008: Understanding the local and global impacts of model physics changes: An aerosol example. *Quart. J. Roy. Meteor. Soc.*, **134**, 1479–1497, doi:10.1002/qj.298.
- Ryan, B. F., K. J. Wilson, and E. J. Zipser, 1989: Modification of the thermodynamic structure of the lower troposphere by the evaporation of precipitation ahead of a cold front. *Mon. Wea. Rev.*, **117**, 138–153.
- Schättler, U., G. Doms, and C. Schraff, 2008: A description of the nonhydrostatic regional COSMO-model, part VII: User's guide. Deutscher Wetterdienst Rep. COSMO-Model 4.11, 142 pp.
- Schepanski, K., I. Tegen, B. Laurent, B. Heinold, and A. Macke, 2007: A new Saharan dust source activation frequency map derived from MSG-SEVIRI IR-channels. *Geophys. Res. Lett.*, **34**, L18803, doi:10.1029/2007GL030168.
- Schultz, D. M., 2005: Review of cold fronts with prefrontal troughs and wind shifts. *Mon. Wea. Rev.*, **133**, 2449–2472.
- , and R. J. Trapp, 2003: Nonclassical cold-frontal structure caused by dry subcloud air in northern Utah during the Intermountain Precipitation Experiment (IPEX). *Mon. Wea. Rev.*, **131**, 2222–2246.
- Shao, Y., A. H. Fink, and M. Klose, 2010: Numerical simulation of a continental-scale Saharan dust event. *J. Geophys. Res.*, **115**, D13205, doi:10.1029/2009JD012678.
- Slingo, A., and Coauthors, 2006: Observations of the impact of a major Saharan dust storm on the atmospheric radiation balance. *Geophys. Res. Lett.*, **33**, L24817, doi:10.1029/2006GL027869.
- Smith, R. K., and M. J. Reeder, 1988: On the movement and low-level structure of cold fronts. *Mon. Wea. Rev.*, **116**, 1927–1944.
- Stanelle, T., B. Vogel, H. Vogel, D. Baeumer, and C. Kottmeier, 2010: Feedback between dust particles and atmospheric processes over West Africa during dust episodes in March 2006 and June 2007. *Atmos. Chem. Phys.*, **10**, 10 771–10 788, doi:10.5194/acp-10-10771-2010.
- Stier, P., and Coauthors, 2005: The aerosol-climate model ECHAM5-HAM. *Atmos. Chem. Phys.*, **5**, 1125–1156.
- Tanaka, T. Y., and M. Chiba, 2006: A numerical study of the contributions of dust source regions to the global dust budget. *Global Planet. Change*, **52** (1–4), 88–104, doi:10.1016/j.gloplacha.2006.02.002.
- Tegen, I., and I. Fung, 1995: Contribution to the atmospheric mineral aerosol load from land surface modification. *J. Geophys. Res.*, **100** (D9), 18 707–18 726.
- , S. P. Harrison, K. Kohfeld, I. C. Prentice, M. Coe, and M. Heimann, 2002: Impact of vegetation and preferential source areas on global dust aerosol: Results from a model study. *J. Geophys. Res.*, **107**, 4576, doi:10.1029/2001JD000963.
- , M. Werner, S. P. Harrison, and K. E. Kohfeld, 2004: Relative importance of climate and land use in determining present and future global soil dust emission. *Geophys. Res. Lett.*, **31**, L05105, doi:10.1029/2003GL019216.
- , B. Heinold, M. Todd, J. Helmert, R. Washington, and O. Dubovik, 2006: Modelling soil dust aerosol in the Bodélé depression during the BoDEX campaign. *Atmos. Chem. Phys.*, **6**, 4345–4359.
- Textor, C., and Coauthors, 2006: Analysis and quantification of the diversities of aerosol life cycles within AeroCom. *Atmos. Chem. Phys.*, **6**, 1777–1813.

- Thorpe, A. J., and C. A. Nash, 1984: Convective and boundary layer parametrizations in a diagnostic model of atmospheric fronts. *Quart. J. Roy. Meteor. Soc.*, **110**, 443–466, doi:10.1256/smsqj.46408.
- Tiedtke, M., 1989: A comprehensive mass flux scheme for cumulus parameterization in large-scale models. *Mon. Wea. Rev.*, **117**, 1779–1800.
- Todd, M. C., R. Washington, S. Raghavan, G. Lizcano, and P. Knippertz, 2008: Regional model simulations of the Bodélé low-level jet of northern Chad during the Bodélé Dust Experiment (BoDEx 2005). *J. Climate*, **21**, 995–1012.
- Tompkins, A. M., C. Cardinali, J.-J. Morcrette, and M. Rodwell, 2005: Influence of aerosol climatology on forecasts of the African Easterly Jet. *Geophys. Res. Lett.*, **32**, L10801, doi:10.1029/2004GL022189.
- Tulet, P., M. Mallet, V. Pont, J. Pelon, and A. Boone, 2008: The 7–13 March 2006 dust storm over West Africa: Generation, transport, and vertical stratification. *J. Geophys. Res.*, **113**, D00C08, doi:10.1029/2008JD009871.
- Weisman, M. L., and R. Rotunno, 2004: “A theory for strong long-lived squall lines” revisited. *J. Atmos. Sci.*, **61**, 361–382.
- White, B. R., 1979: Soil transport by winds on Mars. *J. Geophys. Res.*, **84** (B9), 4643–4651.
- Yin, Y., and L. Chen, 2007: The effects of heating by transported dust layers on cloud and precipitation: A numerical study. *Atmos. Chem. Phys.*, **7**, 3497–3505.